Instruments and Methods

Impedance measurements of the complex dielectric permittivity of sea ice at 50 MHz: pore microstructure and potential for salinity monitoring

Daniel PRINGLE,[1,2] Guy DUBUIS,[3] Hajo EICKEN[1]

[1]*Geophysical Institute, University of Alaska Fairbanks, 903 Koyukuk Drive, Fairbanks, Alaska 99775-7320, USA*
E-mail: pringle@gi.alaska.edu
[2]*Arctic Region Supercomputing Center, University of Alaska Fairbanks, PO Box 756020, Fairbanks, Alaska 99775-6020, USA*
[3]*Institut de Physique de la Matière Complexe, Ecole Polytechnique Fédérale de Lausanne, CH-1015 Lausanne, Switzerland*

ABSTRACT. We report impedance measurements of the complex dielectric permittivity $\varepsilon = \varepsilon' - j\varepsilon''$ of sea ice and laboratory-grown NaCl single crystals using 50 MHz Stevens Water Monitoring Systems Hydra Probes. Temperature cycling of the single-crystal samples shows hydrohalite precipitation, and hysteresis in ε' and ε'' qualitatively consistent with the expected evolution of brine-inclusion microstructure. Measurements parallel and perpendicular to intra-crystalline brine layers show weak (<10%) anisotropy in ε' and a 20–40% difference in ε'' due to enhanced d.c. conductivity along the layers. Measurements in landfast, first-year ice near Barrow, Alaska, USA, indicate brine motion in warming ice as the brine volume fraction v_b increases above 5%. Plots of v_b derived from salinity profiles against ε' and ε'' for these and previous measurements display too much variability between datasets for unguided inversion of v_b. Contributing to this variability are intrinsic microstructural dependence, uncertainties in v_b, and sub-representative sample volumes. A standard model of sea-ice permittivity is inverted to derive the apparent brine-inclusion aspect ratio and bulk d.c. conductivity at a spatial scale complementary to previous measurements. We assess Hydra Probe performance in high-salinity environments and conclude that they are not generally suited for autonomous sea-ice salinity measurements, partly due to the range of relevant brine pocket inclusion length scales.

1. INTRODUCTION

Operational monitoring of sea-ice conditions at local and regional scales using both satellite remote-sensing and in situ observations is gaining in importance. Reasons include increased interest in polar and global climate change, economic activity such as Arctic marine shipping and natural resource extraction, increased scientific operations, and the importance of the ice cover for coastal communities and polar ecosystems. The dielectric permittivity is relevant to both remote-sensing and in situ observations. It governs the interaction between sea ice and an applied electric field and depends on the microscopic composition of sea ice: the volume fractions and geometry of brine and gas inclusions (Hallikainen and Winebrenner, 1992). Here we discuss measurements of the complex permittivity at 50 MHz using commercial in situ sensors, with dual aims: to assess the use of these sensors for automated salinity measurements and monitoring of the state of the ice cover, and to investigate the microstructural dependence of the permittivity at this frequency in the context of modeling dielectric and other sea-ice transport properties (e.g. Golden and Ackley, 1981).

Sea ice is composed largely of pure ice and inclusions of brine and gas, as well as solid salts at temperatures below their precipitation points. Bulk properties, such as permittivity, with a pronounced contrast between brine and ice can depend strongly on the relative volume fractions of ice and brine and their geometric arrangement. Ice temperature and salinity serve as state variables from which the relative brine volume fraction v_b and then other properties can be calculated using established models (e.g. Weeks and Ackley, 1986). In situ temperatures are easily measured, but in situ measurements of salinity are challenging and mostly lacking, although recent advances such as in the work of Notz and others (2005) hold considerable promise.

We report and analyze permittivity measurements at 50 MHz in naturally growing first-year sea ice and laboratory-grown single crystals of NaCl ice. The field measurements are sensitive to the processes in the natural seasonal cycle, and we are particularly interested in identifying potential signatures of enhanced connectivity of brine inclusions, as brine volume fractions exceed the proposed percolation threshold of $v_b \approx 5\%$ (e.g. Golden and others 1998, 2007). The laboratory measurements are sensitive to smaller-scale intra-crystalline effects, microstructural evolution and anisotropy.

These measurements have been made using commercial 50 MHz impedance probes, Stevens Water Monitoring Systems Hydra Probes (hereafter 'hydraprobes'). Hydraprobes are robust, affordable and easily deployed for automated remote operation, and their potential for in situ ice salinity measurements was identified in previous work by Backstrom and Eicken (2006). We extend that work by considering both the real and imaginary parts of the complex permittivity and by examining effects of microstructure in oriented single crystals. New measurements in landfast, first-year sea ice near Barrow, Alaska, USA, are compared with previously reported data. We evaluate probe

https://doi.org/10.3189/002214309788608903 Published online by Cambridge University Press

reliability and accuracy in sea-ice (and saline permafrost) measurements, important considerations as hydraprobes were originally developed for soil moisture measurements at higher temperatures and lower salinities than those examined here.

Following a brief review of the complex permittivity of sea ice at radio and microwave frequencies, we describe the hydraprobe operation and assess their accuracy for sea-ice measurements. We then describe methods and results from laboratory and field measurements. Our analysis includes inversion of the ellipsoidal inclusion model of Tinga and others (1973) to track the inclusion geometry (apparent inclusion aspect ratio), and d.c. electrical conductivity. We make comparisons with previous measurements and assess hydraprobe utility for automated salinity measurements.

2. DIELECTRIC PERMITTIVITY OF SEA ICE

The interaction of sea ice with an applied electric field is governed by its complex relative dielectric permittivity, $\varepsilon = \varepsilon' - j\varepsilon''$. The real part, ε', can in principle be thought of as related to the capacitive response of a material and is sometimes referred to as the 'dielectric constant'. Likewise, the imaginary part, ε'', is related to the conductive response and sometimes called the 'loss factor'.

The permittivity of pure ice, ε_i, is dominated by the orientational relaxation of molecular dipoles with a Debye frequency of about 10 kHz. Around 50 MHz, $\varepsilon_i \approx 3.17$ and $\varepsilon'' \approx 10^{-2}$–$10^{-3}$ are only weakly dependent on frequency. (They also depend weakly on temperature through the relaxation time.) Pure water displays a Debye dipole relaxation at 10 GHz, with a value at 50 MHz that is close to its low-frequency limit, $\varepsilon_{w0}' \approx 80$ (e.g. Addison 1969, 1970; Santamarina and others, 2001). The strong contrast between dielectric properties of water and ice, particularly at microwave frequencies, makes ε sensitive to the fraction of liquid water, and enables the identification of different ice types with remote-sensing methods.

Despite initial work by Addison (1969, 1970), a complete understanding of the overall frequency spectrum $\varepsilon(\omega)$ and the responsible physical mechanisms is lacking for sea ice (Hallikainen and Winebrenner, 1992). Both measurements and theory have focused on the GHz frequencies most relevant to remote sensing. Mixing models show an overall response characterized by an increase in the pure-water relaxation frequency depending on the inclusion geometry, size and inclination with respect to the applied field, and a smearing-out due to their variations (e.g. de Loor, 1968; Hoekstra and Cappillino, 1971). Such models (e.g. Addison, 1970; Tinga and others, 1973; Vant and others, 1978; Arcone and others, 1986) have been fitted to measurements at GHz frequencies with reasonable success, and semi-empirical correlations between ε', ε'' and the brine volume fraction have been established at radar frequencies (Hoekstra and Cappillino, 1971; Vant and others, 1978; Hallikainen and Winebrenner, 1992). The success of these approaches at GHz frequencies is essentially due to the proximity to the water relaxation peak so that the largest effects of brine inclusions are volumetric and geometric. Although tunable by the choice of parameters to describe inclusion geometry (e.g. angle of inclination and ellipsoidal aspect ratios), these models do not capture processes other than orientational relaxation and bulk conductivity. At MHz and lower frequencies, surface conductivity (10^3–10^9 Hz) and relaxation of bound water (10^6–10^9 Hz) might also be expected (de Loor, 1968; Santamarina and others, 2001). In fact, interfacial effects are most pronounced in composites of materials with different conduction mechanisms (Santamarina and others, 2001) such as the case for ice (protonic) and brine (ionic) in sea ice. Little work has been done to characterize these processes in sea ice, due to the focus on GHz frequencies for remote sensing, but it has been noted that their omission from sea-ice permittivity models may explain worse model performance below 500 MHz compared with GHz frequencies (Vant and others, 1978).

The use of dielectric measurements to measure brine volume fraction v_b, and therefore bulk salinity S, relies on the existence of a simple relationship between ε' and/or ε'' and v_b. At GHz frequencies, good correlations ($r^2 = 0.7$–0.8) have indeed been reported for fits to laboratory and field measurements, primarily with functional forms: $\varepsilon' = a_0 + a_1 v_b$, $\varepsilon' = \varepsilon'_i/(1 - 3v_b)$ or $\varepsilon' = a_0 + a_1/(1 - 3v_b)$ (Hoekstra and Cappillino, 1971; Vant and others, 1978; Arcone and others, 1986; Hallikainen and Winebrenner, 1992). From initial hydraprobe measurements at 50 MHz, Backstrom and Eicken (2006) reported a similar linear correlation, $\varepsilon' = 5.15 + 88.50 v_b$. This raised the possibility of using hydraprobes to monitor salinity evolution by measuring ε' and calculating S from temperature and brine volume fractions. This prompted our further investigations here.

The microstructural control of the permittivity was first observed in on-ice radar soundings which showed an anisotropic response for sea ice in which the basal layer displays a strong degree of crystallographic alignment (Campbell and Orange, 1974; Kovacs and Morey, 1978). Prevailing under-ice currents can lead to the alignment of ice lamellae perpendicular to the current, i.e. c axes parallel to the current (e.g. Kovacs and Morey, 1978). On-ice measurements at 100–300 MHz of Kovacs and Morey (1978, 1979) showed weak or no impulse returns when the linearly polarized electric field **E** was tangential to the brine/ice interface (i.e. $\mathbf{E} \perp c$ axis), and strong returns when **E** was normal to the brine/ice interface (i.e. $\mathbf{E} \parallel c$ axis). Golden and Ackley (1981) showed these results to be consistent with the ellipsoidal-inclusion model of Tinga and others (1973). However this ellipsoidal model is not appropriate for extended brine layers in the few-cm-thick skeletal layer at the base of the ice (Golden and Ackley, 1981), and recent X-ray tomography reveals a structure much more complicated than ellipsoidal inclusions even in colder columnar ice (Golden and others, 2007). To examine these effects, we have made directional measurements in single crystals of NaCl ice frozen around in situ hydraprobes.

3. METHODOLOGY

3.1. Hydraprobes

The Stevens Water Monitoring Systems Hydra Probes are impedance devices originally developed for soil moisture measurements (Campbell, 1988, 1990; Stevens Water Monitoring Systems, 2005). The probe consists of a 4 cm diameter cylindrical head with a flat front face from which four parallel 0.3 cm diameter tines protrude 5.8 cm. A central tine is electrically isolated from three equally spaced, surrounding tines (Fig. 1). These tines approximate a coaxial transmission line whose impedance is a function of the permittivity of the material in the sensing volume between

https://doi.org/10.3189/002214309788608903 Published online by Cambridge University Press

the tines. The total impedance of the probe and sample is measured from the reflection of a 50 MHz signal generated in the probe head and transmitted to the tines, and ε' and ε'' are calculated using the known properties of the probe. Of note to our measurements is that the electric field, **E**, is radial from the central tine, i.e. in the plane perpendicular to the direction of the tines. Descriptions of the probe operation, and its accuracy and calibration in soil measurements, can be found in Campbell (1990), Seyfried and Murdock (2004) and Seyfried and others (2005).

Campbell Scientific CR10X data loggers were used to power the probes and record output in the form of four voltage levels. Proprietary software run on a personal computer calculates ε' and ε'' from three of these voltages, and probe temperature from the fourth. Soil water content and soil water salinity are also output using inbuilt conversions for several different soil classes. We ignore those values and analyze only the permittivity and temperature. The next generation of probes, not used here, performs this processing on board. The probes pull 50 mA during measurements, and in field measurements we observed temperature shifts due to self-heating of up to 0.3°C (see below). Probe temperatures in laboratory measurements also showed self-heating and were furthermore inaccurate due to operation close to or below the lower limit of the temperature calibration range, –10°C to +65°C. Independent thermistors were either used directly or calibrated against as described below.

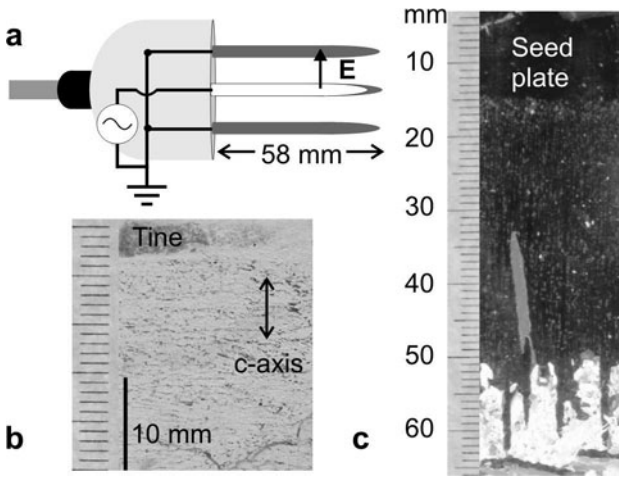

Fig. 1. (a) Hydraprobe schematic. The electric field **E** is circularly polarized between the central and outer tines. The white central tine obscures the third outer tine, whose connection is omitted in the circuit sketch. Tine diameter is 3 mm. (b) Horizontal thin section after experiment A, showing alignment and brine layer spacings of approximately 0.7 mm. (c) Vertical thin section under cross-polarizers after experiment A. The view direction is down tines towards the probe face, i.e. the section is perpendicular to the tines. Crystals growing from the side walls predominate below 55 mm, outside the sensing volume.

3.2. Hydraprobe accuracy and reliability

For the original application of water-content measurements (Campbell, 1988, 1990) in solids with higher temperatures and lower salinities than typical of sea ice, the manufacturers specify the following (Stevens Water Monitoring Systems, 2005): (1) *Calibration and accuracy*: Accuracy of components ε' and ε'' is typically ±1% or 0.5, whichever is greater. Particularly when one component is much larger than the other (five times or more), the accuracy of the smaller component will be degraded, and in general will be 3–5% of the larger value. (2) *High-salinity materials*: When $\varepsilon''/\varepsilon' > 2$, the accuracy of ε' will be degraded. In 'extremely saline soils' where $\varepsilon'' \gg 150$, the value of ε' becomes increasingly inaccurate. Using $\varepsilon'' = \sigma/\varepsilon_0\omega$, where $\varepsilon_0 = 8.85 \times 10^{-12}\,\mathrm{F\,m^{-1}}$ is the permittivity of free space, and ω the angular frequency, this corresponds to a conductivity $\sigma > 0.4\,\mathrm{S\,m^{-1}}$. For $\varepsilon'' > 300 (\sigma > 0.8\,\mathrm{S\,m^{-1}})$, all but soil temperature data become completely unreliable.

The reason for the second condition is that the impedance of high-salinity materials is essentially resistive. Impedance reflection/transmission measurements therefore have high uncertainties in measuring the smaller capacitive component from which ε' is derived. As discussed below, the conditions for accurate performance are met for most, but not all, of our measurements. Cross-borehole resistivity tomography at this location shows that the condition $\sigma < 0.4\,\mathrm{S\,m^{-1}}$ is met at all times except during initial freeze-up (Ingham and others, 2008).

To evaluate the accuracy and reliability of the probes in sea ice, we first performed measurements in deionized water and solutions of NaCl with salinities of 1, 5 and 20 ppt, from 25°C to the freezing point. Two separate samples were used for each concentration, with one probe in each, and temperatures measured with independent thermistors. The results are summarized in Table 1. Between 0 and 25°C the variation was close to linear in all cases. The results for deionized water are as expected, and consistent with those

Table 1. Measured permittivity of NaCl solutions

Salinity ppt	σ(25°C)* $\mathrm{S\,m^{-1}}$	ε'(0°C)†	ε'(25°C)	ε''(0°C)	ε''(25°C)	$\varepsilon''_{\mathrm{calc}}$(25°C)‡
0.0	0.003	93 ± 0.5	82.5 ± 0.5	–1.5 ± 0.5	0 ± 0.5	0
1.0	0.19	92 ± 0.5	80 ± 1	42 ± 1	76 ± 1	68
5.1	0.89	111 ± 1	163 ± 2	115 ± 5	125 ± 5	320
20.4	3.10	156 ± 2	215 ± 5	37 ± 1	50 ± 2	1114

Note: $S = 0.0$ ppt is deionized water.
*Electrical conductivity measured with YSI 30, Handheld Salinity, Conductivity & Temperature System.
†Uncertainties here include only measurement variability and not manufacturer-specified accuracy (see section 3.2).
‡The predicted loss factor at 50 MHz due to electrical conductivity was calculated as $\varepsilon''_{\mathrm{calc}} = \sigma/\varepsilon_0\omega$, where σ is the conductivity measured at 25°C.

https://doi.org/10.3189/002214309788608903 Published online by Cambridge University Press

of Seyfried and Murdock (2004). The probe manufacturers claim adequate performance if $\varepsilon'(25^\circ\mathrm{C})$ is approximately 80, as seen here. The decrease of ε' with temperature reflects the expected temperature dependence of the Debye relaxation time (e.g. Morey and others, 1984). As 50 MHz is well below the ~10 GHz Debye frequency of liquid water, $\varepsilon'' \approx 0$ is expected for pure water. Values measured from 25°C to 0°C decreased monotonically from 0 ± 0.5 to -1.25 ± 0.5. Negative values here are non-physical, and these results illustrate the loss of accuracy when one component is much larger than the other, in this case $\varepsilon' \gg \varepsilon''$. The error in the smaller component (ε'') is about 1% of the value of the larger component (ε'), consistent with specification (1) above.

For water at 50 MHz, the addition of dissolved salts increases the effective loss factor $\varepsilon''_{\mathrm{eff}}$ via enhanced ionic conduction according to $\varepsilon''_{\mathrm{eff}} = \varepsilon'' + \sigma/\varepsilon_0\omega$, but with little effect on ε' (Hoekstra and Cappillino, 1971). Indeed our results show little change in ε' from $S = 0$ ppt to $S = 1$ ppt for which $\varepsilon' \approx \varepsilon''$ and the conditions for reliable measurements are met. From the measured conductivity, the predicted conductive contribution is $\sigma/\varepsilon_0\omega = 68$, close to the measured value of $\varepsilon'' = 76 \pm 1$. However, for $S = 5$ ppt and $S = 20$ ppt, measurements of ε' and ε'' are not consistent with physical expectations: ε' nearly doubled from $S = 1$ to $S = 20$ ppt, and measured values of ε'' did not scale in proportion to conductivity. The predicted and measured loss factors are vastly different, with $\varepsilon''(25^\circ\mathrm{C})$ actually decreasing from 125 ± 5 for $S = 5$ ppt, to 50 ± 2 for $S = 20$ ppt (and similarly at 0°C). This considerable loss of accuracy at high salinities, for which ε'' is expected to be more than several times larger than ε', is consistent with the findings of Seyfried and Murdock (2004) who found little change in ε' for $\sigma < 0.14\ \mathrm{S\,m^{-1}}$ but a loss of accuracy and inter-sensor reproducibility in both ε' and ε'' by $\sigma = 0.28\ \mathrm{S\,m^{-1}}$ (approximately $S = 1.5$ ppt).

With respect to our measurements in ice grown from sea water with $S \approx 34$ ppt and NaCl solutions with $S = 27$ ppt, these results suggest caution in interpreting both ε' and ε'' values until the probes are surrounded by ice of sufficiently low bulk conductivity to avoid the condition $\varepsilon'' \gg \varepsilon'$. The need for caution is underlined in that this loss of accuracy actually affects the apparent value of $\varepsilon''/\varepsilon'$. The inverse condition, $\varepsilon' \gg \varepsilon''$ seen for deionized water does not apply to the present work.

3.3. Inversion of ellipsoidal inclusion model

To relate our measurements to brine inclusion geometry, we have inverted an ellipsoidal inclusion permittivity model. Following Vant and others (1978), we consider the ellipsoidal inclusion model of Tinga and others (1973) using ice and brine properties as specified by Stogryn (1971). We also correct the typographical errors in Vant and others (1978) identified by Farrelly (1982). This model assumes a population of ellipsoidal inclusions with constant aspect ratio, γ = major axis length/minor axis length, inclined at an angle θ with respect to the propagation direction of the incident radiation. In our measurements, this direction is along the tines, so for vertical inclusions $\theta = 90^\circ$, and the variant model of Farrelly (1982) gives the same result as that of Vant and others (1978). We refer to this as the VTS model (for Vant–Tinga–Stogryn).

In this model when θ is fixed, ε' is a unique function of γ, and we have used a converging iterative scheme to determine γ by matching the modeled value $\varepsilon'(\gamma)$ to the measured value ε'. The VTS model does not include bulk conductivity. Therefore the model value of ε'' for the fitted value of γ reflects only polarization. We subtract this from the measured value ε'' to calculate the apparent d.c. conductivity as $\sigma = \varepsilon_0\omega(\varepsilon''_{\mathrm{VTS}} - \varepsilon'')$. For the tolerance between measured and matched values of $\delta\varepsilon' = 0.01$, relative uncertainties in $\delta\gamma/\gamma$ and $\delta\sigma/\sigma$ are less than 0.5%. For likely overestimates of measurement uncertainties of $= 0.1^\circ$C and $\delta\varepsilon' = 0.2$, the fractional uncertainties for γ and σ from model inversion are approximately 5%.

The VTS model returns analytical forms for $\varepsilon(\gamma, \theta)$ at the expense of a highly simplified inclusion geometry (e.g. Golden and Ackley, 1981; Backstrom and Eicken, 2006). Tomographic imaging of single-crystal samples grown in a similar fashion to those in the present work shows that with increasing brine volume fraction, inclusions within intracrystalline brine layers merge to form sub-parallel 'perforated sheets'. As well as an increase in vertical connectivity, these sheets show increased lateral connectivity (Golden and others, 2007). Due to the difference between modeled and actual inclusion geometry, we refer to γ as the 'apparent aspect ratio' and consider it a proxy for the actual geometry.

4. LABORATORY MEASUREMENTS

4.1. Laboratory measurements on single-crystal NaCl ice

In situ measurements were made in a temperature-controlled cold room during the growth of oriented NaCl single crystals around a hydraprobe. Single crystals were grown by seeding NaCl solutions with oriented single crystals of freshwater ice using a method resembling that of Kawamura (1986). Crystallographically oriented seed plates 10–15 mm thick were made from several large single crystals cut from freshwater ice obtained from a local gravel pit in Fairbanks, Alaska. Within the seed plates, *c* axes were oriented parallel in the horizontal plane within ±5°. Alignment was first determined with a universal stage and thin sections microtomed to a thickness of 0.3 mm (Langway, 1958). Several ice pieces were then arranged under cross-polarizers and 'glued' together by freezing a thin layer of deionized water. Salt solutions were prepared at room temperature by dissolving pure NaCl salt in deionized water. Solutions were cooled to just above freezing in the cold room and thoroughly stirred before salinity measurements with an automatic salinometer (YSI 30, Handheld Salinity, Conductivity & Temperature System). With the solution temperature just above freezing, the seed plate was placed on the salt-water surface so that a partial melt-back of the ice sheet would occur to remove imperfections and disoriented crystals due to the ice 'gluing'.

Ice was then grown in a tank of transparent plastic, of width 15 cm, length 26 cm and depth 14 cm. During ice growth, the tank was insulated on five sides by 5 cm thick foam with the upper surface uncovered. This minimized lateral heat flux during ice growth in order to grow ice comparable to natural, columnar first-year sea ice. Outward-flaring container walls allowed upwards ice slip to relieve pressure build-up during growth. A hydraprobe was positioned horizontally with upper tines 1 cm below the bottom surface of the seed plate. Temperature at the depth of the probe center was measured with a thermistor positioned behind the probe head. The thermistor bead was in intimate

https://doi.org/10.3189/002214309788608903 Published online by Cambridge University Press

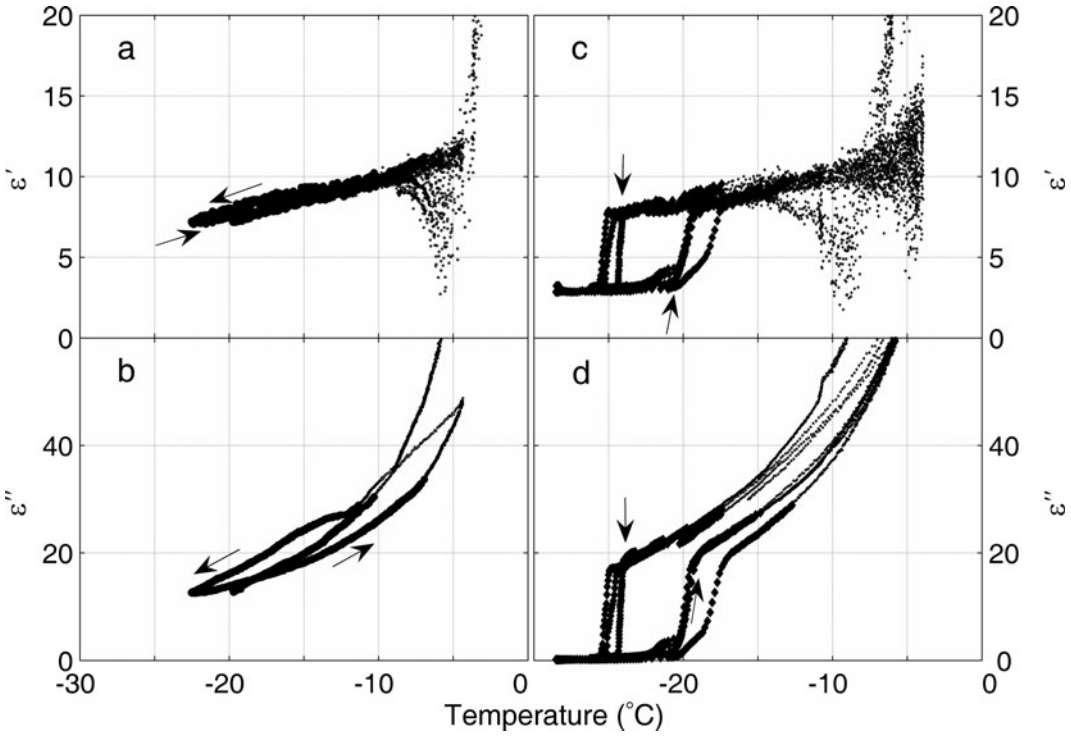

Fig. 2. Measured permittivity for experiment A (a, b) and experiment B (c, d). Arrows indicate trajectory on first cooling and warming cycle. Temperatures in experiment B were low enough to induce precipitation, and then subsequent dissolution of hydrohalite, $NaCl{\cdot}2H_2O$. Larger points are those satisfying $\varepsilon''/\varepsilon' < 3$, and smaller points are all data for $T < -3°C$.

contact with the ice; a second thermistor was positioned 1 cm above the upper ice surface of the seed plate. Hydraprobe and thermistor output were typically logged every 2 min. NaCl ice was grown with an ambient temperature of –10°C until the probe was completely enveloped, after which the temperature was lowered to –20°C to grow ice to the bottom of the tank. Ice temperatures were then cycled by successively setting the ambient cold-room temperature to 0°C and –30°C, with care taken to keep ice temperatures below –3°C in order to avoid complete melting. To monitor ice growth, the vessel was removed at regular intervals from the insulation for inspection and to photograph freezing-front progression. Ice growth around the probe was confined to downward advancement of the ice–water interface, ensuring the formation of a large single crystal (Fig. 1c). Some ice later grew from the lower lateral edges of the tank, indicating lateral heat flow, but the probe measurements were not at all sensitive to the microstructure of this ice outside the sensing volume. Salinity profiles were measured at the completion of each experiment. Thin sections cut in different orientations with respect to the probe head showed the ice grown around the probes to be effectively an oriented single crystal. Figure 1b shows the structure for experiment A, with brine layer spacings of approximately 0.7 ± 0.2 mm, with a similar spacing for experiment B not shown.

Probe orientation can be described with respect to tine direction, applied electric field **E**, crystallographic **c** axis, and platelet/brine inclusion arrangement. These are related by the **c** axis being perpendicular to the ice platelets, and the circularly polarized **E** being radial from the central tine (Fig. 1). In experiment B, the probe tines were parallel to the *c* axis, with **E** parallel to brine layers. This is the 'tangential polarization' configuration of Golden and Ackley (1980). In experiment A, the probe tines were perpendicular to the *c* axis. The vertical component of the circularly polarized **E** is tangential to the brine layers, but the horizontal component is normal to them, a situation intermediate between the tangential and normal polarizations of Golden and Ackley (1980). Post-measurement orientation analysis showed ice platelets in experiment A were highly parallel to the probe, and that in experiment B they were nearly perpendicular (misaligned by 6°).

4.2. Results from single-crystal NaCl ice

Permittivity measurements were made for two different probe orientations in laboratory-grown single crystals of NaCl ice, according to the method described above and with temperature cycles and probe orientations given in Table 2. Results showing the temperature dependence of ε' and ε'' for experiment A are shown in Figure 2a and b, and for experiment B in Figure 2c and d. Only data for $T < -3°C$ are shown. The lighter points are those for which $\varepsilon''/\varepsilon' > 3$ and the heavier points $\varepsilon''/\varepsilon' < 3$; as discussed below, only the latter are considered reliable. The most obvious differences between experiments are the signatures of hydrohalite precipitation below about –20°C in experiment B, which we address below. Other key observations from Figure 2 are:

1. There is hysteresis in $\varepsilon'(T)$ and $\varepsilon''(T)$ for both experiments, with arrows indicating the first cooling and warming cycle. Elevated values during the initial cooling cycle are expected due to the higher salinity and brine volume fraction compared with subsequent cycles for which some brine drainage will have occurred. This difference is more pronounced at higher temperatures, but even below –15°C we observe $\varepsilon'(T)$ during the initial cool-down to be up to 15% higher than subsequent cooling

https://doi.org/10.3189/002214309788608903 Published online by Cambridge University Press

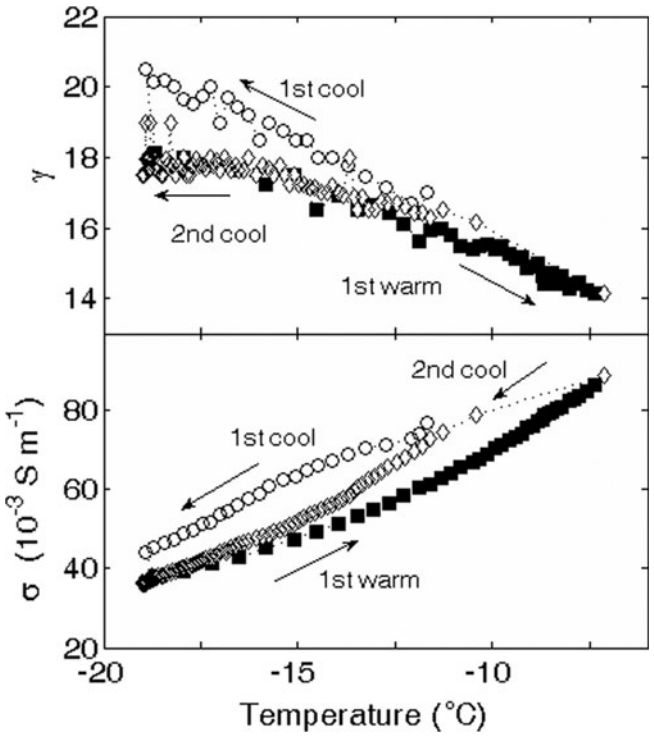

Fig. 3. Results of inverting Vant–Tinga–Stogryn ellipsoidal inclusion model with $\theta = 90°$, for temperature cycles in experiment A. (a) Apparent aspect ratio, γ = major axis/minor axis; (b) d.c. electrical conductivity, σ. At –8°C, $v_b = 5.1 \pm 0.6\%$, and at –18°C, $v_b = 2.5 \pm 0.4\%$. Different legs of heating and cooling cycles have different symbols (see also Fig. 2).

cycles. The difference for ε'' is up to 25% for experiment A and less than 10% for experiment B. We examine subsequent hysteresis in experiment A in terms of the apparent aspect ratio γ below.

2. The local minima and high scatter in $\varepsilon'(T)$, which occur between –10°C and –5°C for both probe orientations, are unexpected and non-physical. Measurements at these and higher temperatures are associated with measured ratios of $\varepsilon''/\varepsilon'$ above 3 and as high as 50. Spurious behavior is consistent with the specification that ε' measurements become unreliable for $\varepsilon''/\varepsilon' > 2$ which is expected here due to high bulk conductivities. Based on the self-consistency of ε' measurements at temperatures below these minima, we consider a slightly higher threshold for reliable measurements to be $\varepsilon''/\varepsilon' \leq 3$. Quite why the loss of accuracy results in minima is unknown, but in section 5.3 we note similar results from probes in first-year sea ice of atypically high salinity.

3. We have measured at most a weak anisotropy in the dielectric constant. Discounting the initial cool-down, Figure 2 shows $\varepsilon'(T)$ approximately $5 \pm 5\%$ higher in experiment B than in experiment A. A much stronger anisotropy is observed in $\varepsilon''(T)$, where values in experiment B (for which **E** is always parallel to the brine layers), with an expected higher conductivity parallel to the brine layers, are 20–40% higher than for the perpendicular geometry in experiment A.

4. A pronounced feature of the plots of Figure 2c and d is the signature of hydrohalite ($NaCl{\cdot}2H_2O$) precipitation in experiment B, for which sufficiently low temperatures were not reached in experiment A. Below the eutectic point, liquid brine is not thermodynamically stable, and water can only exist as ice or as water of hydration in the precipitate. Hence v_b goes to zero, and with little contribution from hydrohalite itself (Addison, 1970) the permittivity approaches that of pure ice, with $\varepsilon(T)' \approx 3$ and $\varepsilon''(T) \approx 0$. The response in natural sea ice will be very similar, where v_b drops to below 1% at –25°C. Our measurements show precipitation commencing below –24°C, lower than the –21.2°C equilibrium precipitation point of hydrohalite in pure NaCl–water solutions (Hall and others, 1988). Dissolution commences at temperatures between –22 and –21°C and is complete by –19°C (except for the cycle with the lowest minimum temperature). Similar hysteresis effects were reported by Addison (1970) and Hoekstra and Cappillino (1971).

The observed supercooling prior to precipitation suggests that the nucleation of hydrohalite requires some supercooling below the equilibrium precipitation temperature and is commensurate with findings by Cho and others (2002) and Light and others (2003). Once hydrohalite has started to form, it proceeds essentially unhindered at a rapid rate as indicated by the steep drop-off in ε'. Dissolution appears to set in at the precipitation point, but, with comparatively rapid heating rates and diffusion constraints, hydrohalite crystals are likely not entirely subsumed until a higher temperature is reached, as corroborated by the shape of the hysteresis curve and the slightly smaller gradient in the ε'–T curves. In the cycle

Table 2. Details of laboratory experiments

Property	Experiment A	Experiment B
NaCl solution salinity (ppt)	27.0	27.7
Tine orientation	Perpendicular to **c** axis	Parallel to **c** axis
Polarization*	E_v // platelets $E_h \perp$ platelets	**E** // platelets 'Tangential'
Temperature cycling (°C)	18 ↘ –22.5	5 ↘ –25.4 ↗ –5.5 ↘ –15.7
	↗ –4.4 ↘ –19.7	–28.5 ↗ –3.9 ↘ –26.3
		↗ –4.3 ↘ –26 ↗ –6
Bulk salinity at probe (ppt)†	7.8 ± 1.0	7.2 ± 0.8
Duration (days)	5	7.2

*Electric field **E** is radial from central tine, with vertical component E_v and horizontal component E_h.
†From conductivity of ice adjacent to probe center, at the end of the experiments.

https://doi.org/10.3189/002214309788608903 Published online by Cambridge University Press

with both the lowest temperature and longest time below the precipitation temperature, the subsequent dissolution occurs at slightly higher temperatures. This could reflect increased coalescence of precipitates.

5. Results from the VTS model inversion for experiment A are shown in Figure 3. For clarity, we plot the mean of every five measurements. Results for experiment B are similar but span a smaller temperature range and are not shown. Figure 3a shows that in general the apparent aspect ratio γ increases as temperature and ε' decrease. As noted in section 3.3, γ is a proxy measure of inclusion geometry. We discuss these results and their broader implications with respect to microstructural evolution and γ in more detail in section 6. Subsequent warming and cooling shows evidence of a weak hysteresis only above –12°C (corresponding to $v_b = 3.5 \pm 0.5\%$). Figure 3b shows a more pronounced hysteresis in the conductivity, with σ(–10°C) approximately 25% higher during recooling than warming, and convergence only for $T \sim <-16$°C ($v_b = 2.8 \pm 0.4\%$). As σ is highly dependent on inclusion connectivity, this suggests a thermal-history dependence of the connectivity: high connectivity persists with cooling but, after disconnection at low temperatures, requires a larger temperature increase to be re-established. Light and others (2003) made direct observations of this process for individual inclusions in natural first-year sea ice.

We do note that while the contribution from d.c. conductivity is expected to be strong at 50 MHz (Hoekstra and Cappillino, 1971), it is possible that ε'' reflects contributions from polarization mechanisms not captured in the VTS model, such as surface-area dependent interface effects (de Loor, 1968; Santamarina and others, 2001). However, unless the relaxation frequency were close to 50 MHz, the contribution to ε'' would be weak. If this were the case, then the aforementioned effects would in part reflect a similar hysteresis effect in the specific surface area. Regardless, either interpretation indicates hysteresis in the non-unique temperature-dependent microstructure.

The points in Figure 3b do not exceed $v_b = 5\%$ (–7.1 ± 1.1°C), so we cannot directly assess percolation theory predictions of a transition in the connectivity in this vicinity. We note that Figure 2b does show an increase in $d\varepsilon''/dT$ above approximately –7.5°C ($v_b \approx 5.2\%$). However, this observation relies on the accuracy of ε'' measurements when $\varepsilon''/\varepsilon' > 3$. Furthermore, in the absence of a direct relationship between conductivity and connectivity, this effect is ultimately only suggestive of an increase in the temperature rate of change of the connectivity.

5. FIELD MEASUREMENTS

5.1. Field measurements in Barrow, Alaska

A vertical array of three hydraprobes was installed in growing landfast first-year sea ice on the Chukchi Sea near Point Barrow in January 2007. This array was one component of an automated 'mass-balance site' operated until mid-June 2007. The site was approximately 300 m offshore at a water depth of approximately 6.5 m. A CR10X data logger provided switched power to the probes, and recorded output.

Hydraprobes were positioned along a 1.5 m long half-pipe of 4 in (10 cm) diameter PVC (Backstrom and Eicken, 2006). The probes were fit tightly in holes drilled in the pipe, with the tines protruding from the convex side at depths of 0.80, 0.95 and 1.10 m. The array was installed through two overlapping 10 cm diameter core holes in 0.69 m thick ice with the tines facing the coast, and therefore perpendicular to the prevailing alongshore current, as in Backstrom and Eicken (2006). The probes were initially below the ice–water interface and were frozen in as the ice grew to a maximum thickness of 1.4 m. During extraction we observed that the ice frozen around the probes was similar to the adjacent ice, with sub-parallel brine layers oriented approximately perpendicular to the tines. We present results from probes B80 (0.80 m) and B95 (0.95 m); the probe at 1.10 m malfunctioned shortly after installation.

Hydraprobe self-heating was evident when the initial measurement interval of 30 min was decreased to 1 min on 17 April. The reduced time for the dissipation of heat during signal generation and measurement led to an abrupt step in the probe temperature of +0.29°C. Decreasing the sampling interval to 5 min on 18 May gave a downwards step of –0.27°C. This is the temperature of a thermistor inside the probe head. Permittivity measurements at these times indicate that this was not accompanied by significant warming or cooling of the ice in the sensing volume. Temperatures were normalized to the measurements with 30 min sampling intervals by applying offsets to reverse these steps. These normalized temperatures were then calibrated against temperatures of the mass-balance site thermistor string less than 10 m away. A warm-water advection event in late January was recorded by the thermistor string and both hydraprobes (which were still in the water column below the ice interface), as shown in Figure 4. All sensors measured temperature excursions with the same magnitude. One-point calibrations were applied to rectify the observed hydraprobe offsets (+0.55°C and +1.1°C). Figure 2a shows the adjusted thermistor temperature–time curves agree very well with the thermistor string measurements.

When the hydraprobes at depths 0.80 and 0.95 m froze in, the ice at the thermistor string site was 0.86 and 1.01 m thick respectively. We therefore use the latter depths to compare the permittivity measurements with ice conditions at the thermistor string site shown in Figure 4. The interpolated temperature field is shown in Figure 4b. Figure 4c shows the brine volume fraction calculated by applying the equations of Cox and Weeks (1983) and Leppäranta and Manninen (1988) to these temperatures, and salinity profiles $S(z)$ determined from cores in late January, late April and early June. These cores showed the characteristic evolution of $S(z)$ for first-year ice (e.g. Weeks and Ackley, 1986; Eicken, 2003). From them we determined a simplified time-dependent, piecewise salinity profile to capture the main variations in depth and time: (1) over the bottom 20 cm, S varied linearly between 15 ppt and 5 ppt; (2) above this, the salinity was constant at 5 ppt until the top 10 cm; (3) over the top 10 cm, S varied linearly between 5 ppt and a time-dependent surface salinity, $S_0(t)$, which decreased smoothly from 15 ppt in late January to 10 ppt in late April and 4 ppt in early June. The same approach was applied to compute v_b for identical hydraprobe measurements in McMurdo Sound, Antarctica, 2002 and Barrow 2003, for which full descriptions are provided by Backstrom and Eicken (2006), and salient details discussed below.

https://doi.org/10.3189/002214309788608903 Published online by Cambridge University Press

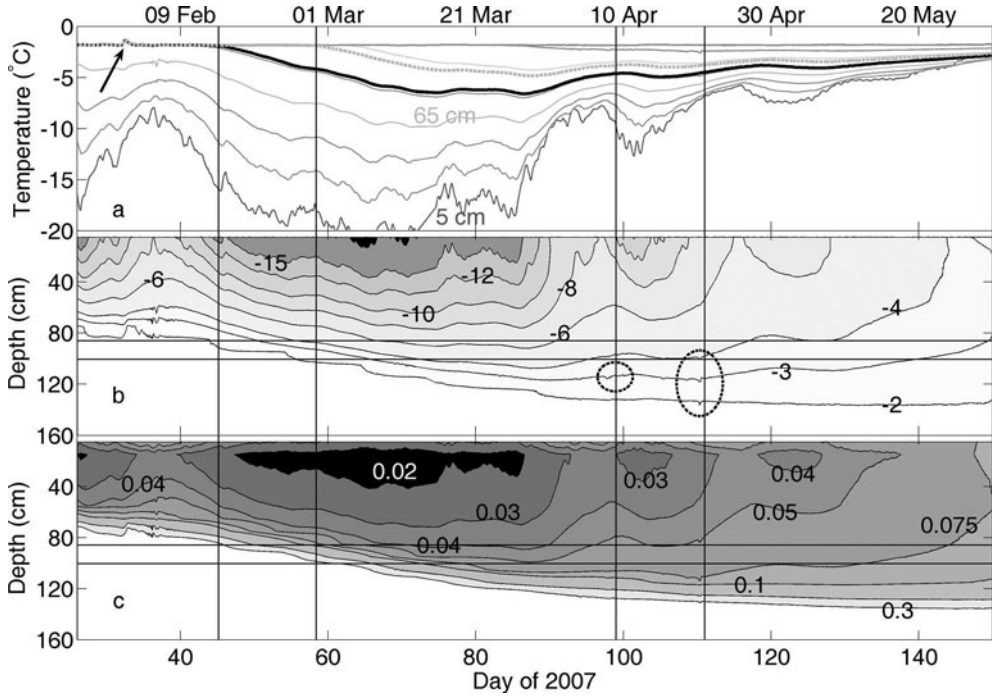

Fig. 4. Ice conditions from 2007 Barrow mass-balance site. (a) Temperature–time traces for every second thermistor (vertical spacing of those shown here is 20 cm). Heavy curves are hydraprobe temperatures: solid is B80 and dashed is B95. Arrow indicates warm-water advection event. (b) Interpolated ice temperatures and isotherms. Ellipses indicate temperature signatures of brine motion (see section 5.2). (c) Calculated brine volume fraction. Horizontal lines are hydraprobe equivalent depths at the thermistor string site. Vertical lines are times of hydraprobe freeze-in times (11 and 27 February) and of brine motion signatures (9 and 21 April).

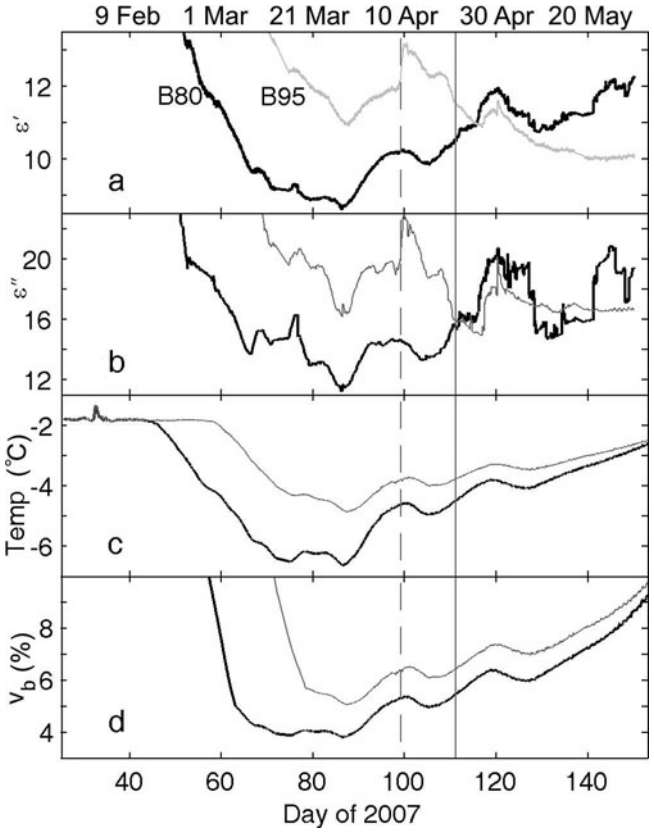

Fig. 5. Time-series results from 2007 Barrow hydraprobes for (a) ε'; (b) ε''; (c) temperature; and (d) calculated brine volume fraction. Apart from temperature, only data after the freeze-in of each probe are shown. Heavy curves are probe B80 (80 cm below the ice surface) and light curves are B95 (95 cm below the ice surface). The dashed line marks 9 April (day 99), and the solid line 21 April (day 111) (see section 5.2).

5.2. Results from Barrow 2007

Results from the hydraprobes in landfast, first-year sea ice in the Chukchi Sea near Barrow in 2007 are shown as time series in Figure 5, and plotted against temperature in Figure 6. The temperature plots clearly show the overall behavior and can be compared with the laboratory results in Figure 2. We first consider the time series, to allow direct comparison of permittivity variations with changes in brine volume and temperature during spring warming.

Figure 5 shows time series for both probes after freeze-in. Figure 5c and d show probe temperatures and brine volume fractions calculated from probe temperatures and time-evolving salinity profiles, according to which $S = 5$ ppt for probe B80 after day 63, and for probe B95 after day 78. For constant bulk salinity, all other things being equal, and the assumption of thermohaline equilibrium, ε' and ε'' will increase with v_b and therefore temperature. Our expectation of ε' and ε'' qualitatively following temperature variations is generally met by probe B80 until day 111 (21 April), and probe B95 until day 99 (9 April). Within the VTS model, a decrease in ε' or ε'' with increasing temperature can result from a decrease in salinity, reduction in aspect ratio γ or change in inclusion orientation from $\theta = 90^\circ$.

After 21 April, but not before, probe B80 shows simultaneous, episodic jumps of $\Delta\varepsilon' \approx \pm 0.1$–$0.2$ and $\Delta\varepsilon'' \approx \pm 1$–$2$. Prior to 21 April was a period of warming during which the brine volume fraction at the depth of B80 increased (Fig. 4). In terms of a threshold, we note that the calculated brine volume fraction here exceeds 5.4% for the first time since freeze-in, and both temperature and v_b are increasing in the ice above the hydraprobes (Fig. 4b). Backstrom and Eicken (2006) noted fluctuations in ε' for similar ice conditions, which are precisely those associated with thermal signatures of brine overturning events. Here

https://doi.org/10.3189/002214309788608903 Published online by Cambridge University Press

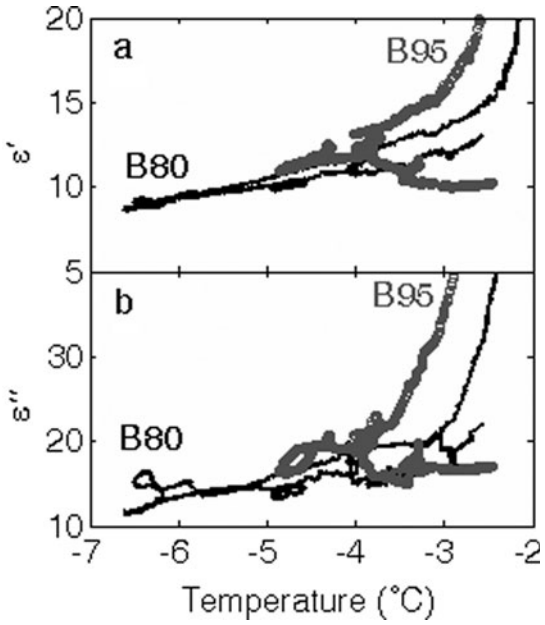

Fig. 6. (a) Dielectric constant ε' and (b) loss factor ε'' from Barrow first-year ice, 2007. Black curves are B80 (80 cm below the ice surface), and small gray circles are B95 (95 cm below the ice surface). During freeze-in the ratio $\varepsilon''/\varepsilon'$ peaked at approximately 3; all plotted data have $\varepsilon''/\varepsilon' \leq 2$.

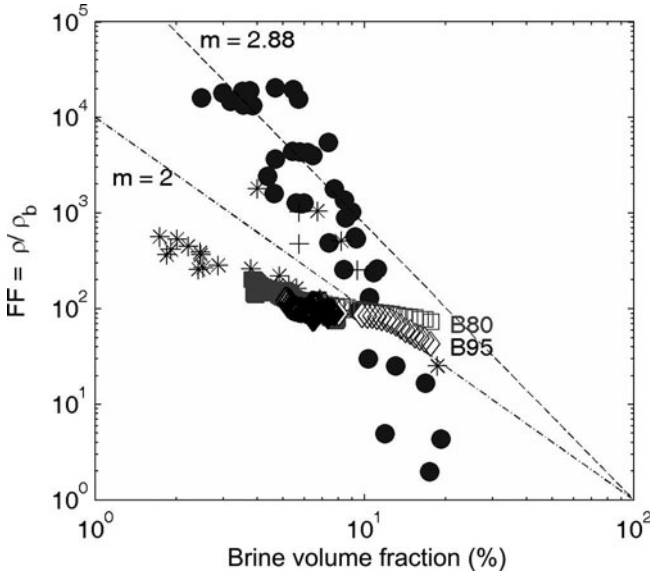

Fig. 7. Formation factor, FF $= \rho/\rho_b$, where ρ_b is brine resistivity, from Barrow 2007 hydraprobe d.c. conductivity (diamonds and squares). The points closest to the labels correspond to probe freeze-in. Solid circles represent borehole resistivity tomography measurements of Ingham and others (2008) at Barrow in 2006. Asterisks are Morey and others (1984), and crosses Buckley and others (1986). Lines indicate Archie's-law behavior, FF $= v_b^{-m}$.

the increase in brine volume and associated connectivity facilitate density-driven brine motion including the drainage of dense surface brine from above the freeboard (Pringle and others, 2007). We therefore attribute jumps in ε' for B80 after 21 April to salinity variations caused by brine movement. This is supported by the thermistor string measurements which clearly show a rare thermal signature of brine movement in the lower thermistors on day 110 (Fig. 4b). We discuss below the inversion of the VTS model for these measurements and compare the derived conductivity measurements with the in situ resistivity measurements of Ingham and others (2008).

Probe B95 exhibits slightly different behavior. On 9 April it showed a sudden increase of $\Delta\varepsilon' \approx +1.1$ and $\Delta\varepsilon'' \approx +3.6$. This followed a surface warming to above –10°C in the previous week causing v_b to exceed 4% in the bottom half of the ice, and the temperature record again shows an overturning signature. As above, we attribute this to brine motion in warming ice, and likewise the pronounced steps on 27 and 30 April of a similar magnitude to those recorded by probe B80. Otherwise, probe B95 shows a decrease in both ε' and ε'' despite increases in temperature, and the brine volume fraction always exceeding 6%. The trend in ε' is most interesting, as it is expected to be less sensitive than ε'' to variations in brine inclusion morphology (Backstrom and Eicken, 2006). We speculate that, if this is not due to sensor malfunction, then a possible explanation may relate to the observation by Cole and Shapiro (1998) of numerous instances of emptied brine channels (i.e. gas-filled). A smaller-scale equivalent could possibly occur if connectivity were suddenly established from within our sensing volume to existing gas-filled inclusions below. If the connectivity to above were not increased, brine would drain downwards, being replaced by gas. Subsequent temperature variations would not cause the expected variations in v_b, and the permittivity would be less than predicted by the no longer applicable composition-based mixing models. This is a particular case of the sensing volume being non-representative of the average bulk properties of the surrounding ice. A more general observation is that the length scales of the tines and sample space are of the order of centimeters, which is small compared to the length or diameter of secondary brine drainage features, or even the length scale over which single crystal brine layers are connected for $v_b > 4\%$ (Golden and others, 2007), so that the measured permittivity can be sensitive to local variations at these scales.

The overall temperature dependence of ε' and ε'' for both probes is shown in Figure 6. It is largely as expected and resembles the laboratory results. The variations in ε' and ε'' discussed in the preceding paragraphs are clear above about –4.5°C: probe B80 generally follows the expected increase with temperature, and B95 shows an anomalous decrease in ε'. Both probes show loops in ε'' and somewhat smaller loops in ε', at times of temperature minima (e.g. the overall minima between days 75 and 90 and the cooling event between days 100 and 110). These loops likely reflect localized brine motion or variations in inclusion salinity and morphology due to time lags during re-equilibration with natural temperature cycling.

From inversions of the VTS model, the probe B80 variations of $\varepsilon'' = 18 \pm 2$ give $\sigma = 0.047 \pm 0.006\,\mathrm{S\,m^{-1}}$ or a bulk sea-ice resistivity of $\rho = 22 \pm 3\,\Omega$m. Resistivity variations of this magnitude are reasonable when compared with cross-borehole resistivity tomography measurements at the same time of year (22–25 April) at our 2006 site in the immediate vicinity (Ingham and others, 2008). Those measurements showed resistivity variations from approximately 10 to 1000 Ωm over the bottom 40 cm of the ice, so that brine motion over distances of the order of centimeters could readily account for the observed ε'' variations.

https://doi.org/10.3189/002214309788608903 Published online by Cambridge University Press

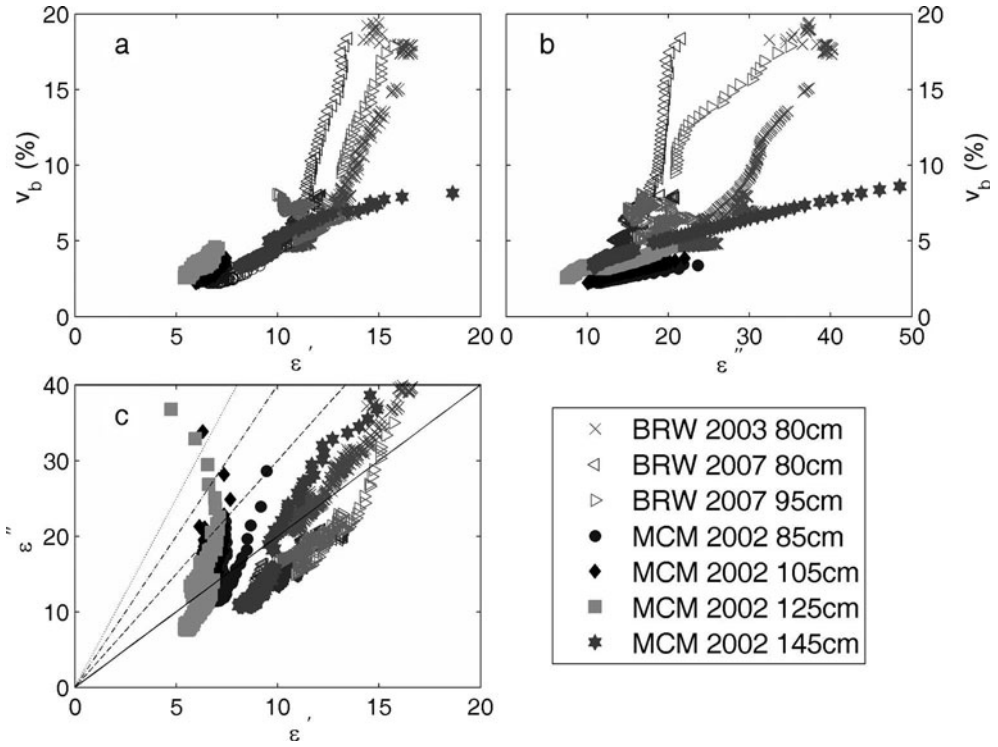

Fig. 8. Compilation of all hydraprobe measurement sets from McMurdo Sound (MCM) and Barrow (BRW). Shown are all measurements satisfying $\varepsilon''/\varepsilon' < 3$ and $T < -3°C$. (a) Calculated brine volume fraction plotted against ε'; (b) v_b plotted against ε''; and (c) ε'' plotted against ε', where straight lines show $\varepsilon''/\varepsilon' = 2, 3, 4, 5$. (a) and (b) show all data satisfying $\varepsilon''/\varepsilon' < 3$ and $T < -3°C$. For clarity, only one point for every 6 hours is plotted. See section 5.3 for discussion of datasets.

For porous media with a bulk resistivity, ρ, that is highly dependent on the connectivity of a high-conductivity pore phase (here brine, with resistivity ρ_b), it is appropriate to consider a formation factor, FF $= \rho/\rho_b$. Figure 7 shows the FF values derived here, along with those from cross-borehole resistivity tomography in similar ice at the same location in 2006 (Ingham and others, 2008). For both datasets, ρ_b is calculated identically following Morey and others (1984) and Leppäranta and Manninen (1988). The points closest to the site labels B80 and B90 correspond to the probe freeze-in. Aside from these points, the present formation factors are lower than the borehole measurements, indicating higher measured conductivities. This is expected on the basis of both electrical anisotropy and, primarily, scale dependence. The hydraprobe measurements are sensitive to brine connectivity over cm-length scales, over which we expect much higher inclusion connectivity than the boreholes' lateral separation of 1 m. Additionally, the borehole measurements are sensitive to the horizontal component of the resistivity ρ_H, so for these points FF $= \rho_H/\rho_b$ (Ingham and others, 2008). The hydraprobes measure the resistivity in the plane perpendicular to the tines, dependent also on the vertical resistivity, ρ_V, which can be smaller than ρ_H by factors of 2–50 due to greater brine connectivity in the vertical direction (Timco, 1979; Buckley and others, 1986; Ingham and others, 2008). The issue of small length scales in hydraprobe measurements of conductivity has been noted by Yoshikawa and others (2004).

5.3. Comparison with measurements in McMurdo Sound 2002 and Barrow 2003

With the aim of evaluating the broader utility of hydraprobes for in situ salinity measurements, and with a better understanding of the accuracy and limitations of the sensors in artificial and natural sea ice, we now compare the Barrow 2007 results with previous field data from McMurdo Sound 2002 and Barrow 2003. Measured values of ε' for the most reliable probes at these two sites were previously presented by Backstrom and Eicken (2006). From plots of $v_b(\varepsilon')$ and the known relation between salinity and brine volume, an empirical fit was derived to allow calculation of S from measurements of ε'. We extend this analysis to all available data and also consider ε''.

The calculated brine volume for these sites is shown in Figure 8a and b as a function of measured ε' and ε'', and Figure 8c shows ε'' plotted against ε'. Figure 8c shows that most data for these probes satisfy $\varepsilon''/\varepsilon' < 3$ but far fewer points satisfy the manufacturer's criteria, $\varepsilon''/\varepsilon' < 2$. The scatter plots for each sensor in Figure 8c converge towards the expected zero-porosity values for these plots, $\varepsilon' \approx 3$ and $\varepsilon'' \approx 0$. The upper sensors in McMurdo Sound show the highest values of $\varepsilon''/\varepsilon'$ and also a minimum in $\varepsilon'(T)$ similar to that observed in the laboratory experiments. This is presumably due to the high salinity of the platelet ice enveloping these probes (Backstrom and Eicken, 2006). We proceed by discussing Figure 8a and b with this microstructural variability in mind, but with an eye towards assessing reliability of the hydraprobes for in situ salinity measurements without the benefit of auxiliary ice characterization.

The high scatter in Figure 8a suggests that for a broader set of measurements a simple conversion between v_b and ε' measured with hydraprobes holds less promise than indicated by the prior analysis of a smaller dataset (Backstrom and Eicken, 2006). Above $v_b \approx 5\%$, there is a high variability between the three Barrow probes and the McMurdo probe at 1.45 m. Results from the Barrow probes show a similar gradient, but with sufficient offsets to introduce large uncertainties in a $v_b(\varepsilon')$ inversion. For example, $\varepsilon' = 13$ was measured for ice with v_b of 6% and 14%. Results from initial

https://doi.org/10.3189/002214309788608903 Published online by Cambridge University Press

cooling of the McMurdo probe at 1.45 m show a clear departure from the Barrow probes above about $v_b = 6.5\%$. At these higher brine volumes, data come either from initial cooling following freeze-in or during spring warming. In both cases, there are physical effects and measurement uncertainties contributing to the observed scatter in Figure 8a and b. The time-series analysis above has already shown episodic abrupt, and sometimes not reversed, steps in ε' and ε'' for $v_b > \sim 6\%$. Furthermore, and more fundamentally, these plots relate measured permittivity values to v_b which is derived rather than measured. Calculations of v_b used a salinity gradient at the base of the ice derived from salinity cores and an interpolated ice thickness. This calculation has its highest uncertainty during probe freeze-in due to uncertainty in the distance of the probe from the bottom of the ice. At –4°C, a not unreasonable uncertainty in the salinity of $S = 8 \pm 2$ ppt gives $v_b = 12.3 \pm 2.5\%$, and part of the scatter in Figure 8a and b surely reflects this source of uncertainty. In summary, the intercomparison of these datasets is confounded by the measurements reflecting variations in microstructure, brine drainage processes and salinity variations within the small sampling volume, and values of v_b derived from average salinities and temperatures.

Figure 8b shows a similar situation for v_b plotted against ε''. As v_b approaches 0, we expect ε'' to go to $\varepsilon''_{ice}(T) \approx 0$ in reasonable agreement with linear fits to the McMurdo probe data (not shown) which give $v_b = 1$–2% when $\varepsilon'' = 0$. However, these data show a factor of 2 difference in v_b for $\varepsilon'' \sim 20$. As in Figure 6a, the Barrow results show a high variability above about $v_b = 5\%$. For individual sensors this is again partially due to the abrupt changes in ε'' during spring warming. Inter-sensor comparison remains complicated by the same concerns as for ε'.

6. DISCUSSION

Considering first the general utility of hydraprobes for assessment of liquid-water fractions in partially frozen media, including permafrost, soils and sea ice, we stress four points: (1) Of six probes deployed in Barrow in 2003 and 2007, two failed for unknown reasons (likely due to extreme temperatures and salinities outside the manufacturer's recommended range of operation), and (likely also as a result of extreme environmental conditions) one out of three laboratory probes gave spurious results (not reported here). (2) Temperature output from the probes is not reliable due to self-heating which depends on the measurement interval. This necessitates independent temperature measurements or careful calibration. The next generation of hydraprobes includes a thermistor in one of the tines, which may reduce this problem. (3) Testing in saline solutions and in artificial and natural ice experiments confirms the manufacturer-specified condition that probe accuracy is compromised for sample conductivity $\sigma > 0.4\,\mathrm{S\,m^{-1}}$. For natural sea ice this is not a severe limitation, as bulk conductivities are lower than this except during freeze-in and in the bottom 10 cm of growing ice. The manufacturer-specified condition for reliable measurements is $\varepsilon''/\varepsilon' < 2$, but from self-consistent laboratory measurements we consider it reasonable to extend this to $\varepsilon''/\varepsilon' < 3$. For higher values of $\varepsilon''/\varepsilon'$, we measured spurious local minima and enhanced noise in $\varepsilon'(T)$ for both laboratory and field measurements in ice with a salinity higher than typical sea ice. (4) The probe dimensions (1–5 cm) are large compared to the primary, sub-millimeter width pore space, but not with respect to the characteristic dimensions of secondary brine inclusions in sea ice, particularly at high brine volumes. For ice warmed above $v_b > 5\%$ in the spring, in which secondary brine features increase in size, there are concerns that the sampling volume is not representative of the surrounding ice. Similar considerations may be relevant for other media.

Within these constraints, laboratory measurements on oriented single crystals of NaCl ice nevertheless gave insight into the microstructural control of the permittivity. After initial ice growth, samples were subject to temperature cycles which revealed hysteretic behavior associated with bulk microstructural changes. Higher values were recorded at the same temperature during cooling compared to warming, with a difference of up to 10% for $\varepsilon'(T)$ and up to 25% for $\varepsilon''(T)$. The larger effect for ε'' is consistent with the expectation that $\varepsilon''(T)$ is more sensitive than $\varepsilon'(T)$ to variations in inclusion morphology (Backstrom and Eicken, 2006), and likely reflects an underlying change in inclusion connectivity. Measurements with the applied electric field **E** parallel to the brine layers gave 20–40% higher values of ε'' than measurements with **E** rotated by 90°. This reflects the higher electrical conductivity expected along the brine layers, rather than across them. Conversely, we measured at most a weak (<10%) anisotropy in ε'. For our geometry this is predicted by the VTS model and expected to be true at least at low temperatures where the assumption of disconnected ellipsoidal inclusions is most reasonable. Measurements to below –23°C showed clear signatures of hydrohalite precipitation and dissolution in successive cycles, along with hysteretic effects. We attribute the latter mostly to supercooling required for hydrohalite crystal nucleation, and to a lesser extent to sluggish dissolution during warming. The difference between first and subsequent cooling cycles was attributed to lower-salinity ice in the later cycles due to brine drainage during growth. However, no signatures of brine drainage events were observed with warming in the laboratory measurements, and although measurements at higher v_b were increasingly unreliable due to the high salinity, this absence may also reflect the absence of the hydraulic head and brine density gradients which drive brine motion in field conditions.

Based on the microscopic and optical observations of Light and others (2003), which showed a slight decrease in aspect ratio with cooling from –5°C to –15°C, we expected similar behavior for the apparent aspect ratio γ returned by the VTS model. Instead, we observed an increase in γ with decreasing temperature. A simple interpretation of this is a change in geometry as brine sheets present at high temperatures dissociate with cooling and separate into more isolated, elongated inclusions. We now examine the interpretation of these γ values in more detail.

The samples of Light and others (2003) were cut from cores of first-year ice extracted near Point Barrow in May 1994, with imaged sections corresponding to in situ temperatures of approximately –4°C and $v_b \approx 5$–6%. Following freezing to –20°C and less for transport and storage, $80 \times 80 \times 2$ mm sections were cut and imaged. At –15°C and for measured lengths l (mm) from 0.03 to 10 mm, they measured aspect ratios between approximately 1 and 50 with a power-law distribution $\gamma(l) = 10.3 l^{0.67)}$. Combined with their power-law fit for number density, $N(l) = 0.28 l^{-1.96}$, this gives an aspect ratio distribution of

https://doi.org/10.3189/002214309788608903 Published online by Cambridge University Press

$N(\gamma) = 257\gamma^{-0.47}$. Using the above limits of $\gamma = 1 - 50$, the first moment of this distribution gives a mean of $\gamma_m = 2.03$, nearly a factor of 10 smaller than our derived values at >–15°C. While we have inverted our measurements with a highly simplified inclusion model, Light and others (2003) also assume an ellipsoidal geometry, recording length and aspect ratio assuming rotational symmetry. One key difficulty in interpreting and comparing these results is the different optical resolutions and sampling volumes which can lead to significant deviations in the derived microstructural variables. In a magnetic-resonance imaging study, Eicken and others (2000) found aspect ratios in the vertical ranging between <2 and >6 depending on the spatial scale considered. This problem is aggravated by the fact that samples analyzed by Light and others (2003) had already been cooled to temperatures well below –20°C at the onset of their experiments. This latter issue is less of a concern for the results of Cole and Shapiro (1998). They obtained micrographic imaging within 1 hour of extraction of similar Chukchi sea ice near Barrow and found vertical aspect ratio distributions with means of 1.5–3, albeit again at a substantially different (smaller) scale.

On the basis of these comparisons, and considering not just the mean values but also the inclusion geometry distributions of Perovich and Gow (1996), Cole and Shapiro (1998) and Light and others (2003), it now seems highly unreasonable to expect a single fitted geometric parameter to both parameterize the average permittivity and provide a simple microstructural interpretation. We ultimately consider γ a proxy parameter and useful in that Figure 3a allows qualitative discussion of microstructure variations and hysteresis. Its particular merit derives from the fact that this inversion approach circumvents the problems deriving from different optical resolutions and hence scale validity of the other datasets referred to above.

Concurrent imaging and hydraprobe measurements may enable a more direct interpretation of γ in terms of inclusion characterization, and possibly allow an assessment of the applicability of the VTS model at 50 MHz. In this model, large aspect ratio inclusions contribute more than small ones. Therefore the omission of polarization mechanisms other than ice and water relaxation would lead to an overestimation of γ when inverting measurements such as ours. However, unless these polarization mechanisms occurred very close to 50 MHz they would affect the predicted value of ε' but not ε'', and not therefore our derived value of the d.c. conductivity.

Measurements in growing, landfast first-year sea ice near Barrow between late January and June 2007 complement earlier measurements in McMurdo Sound in 2002, and Barrow in 2003. The new measurements revealed abrupt, episodic changes in ε' and ε'' during spring under conditions previously identified with convective events, specifically spring warming that drove an increase in the porosity at and above the measurement depth to values above about 5.5%. These events coincided with thermal signatures of brine motion recorded by a nearby thermistor string, and represent brine drainage enabled by increased inclusion connectivity. The variations in ε'' are attributed to conductivity changes due to the instantaneous passage of higher-salinity brine from the colder overlying ice, and subsequent increase in brine volume and connectivity as this brine re-equilibrates to the higher local ice temperature, melting ice and increasing the bulk salinity. Relating variations in ε'' to conductivity by inverting the VTS model, and comparison with the independent cross-borehole resistivity measurements of Ingham and others (2008), gave resistivity variations corresponding to brine transport over vertical distances of the order of centimeters. As expected due to scale and electrical anisotropy, hydraprobe-measured conductivities on the centimeter scale are higher than the meter-scale horizontal conductivity measured at the same site in 2006 (Ingham and others, 2008).

Earlier work of Backstrom and Eicken (2006) suggested a linear relation between brine volume fraction and the dielectric constant, and therefore the potential for using hydraprobes for automated salinity measurements. However, a comparison of our latest measurements with all previous measurements in Barrow and McMurdo Sound reveals scatter between datasets which is too large for accurate inversion. These problems are less pronounced in cold ice, but this ice is of less interest in operational monitoring than warming spring ice for which the scatter is highest. The principal factor that undermines the broader use of hydraprobes for measuring S from ε' is physical variations in ε' due to differences in pore microstructure as a function of ice type and texture. An extreme example of this is the upper probes deployed in McMurdo Sound which were encased in high-salinity platelet ice. Such microstructural variations are likely to result in a different relationship between measured ε' and calculated v_b and hence a different apparent $v_b(\varepsilon')$ curve. Although the measurements from any given hydraprobe could be interpreted in terms of a reasonable conversion for $v_b(\varepsilon')$, the scatter between sensors highlights the difficulty in reducing uncertainties in measuring ε' and calculating v_b from one probe to the next. The quantitative impact of such variations is illustrated in Figure 3a where even in the most homogeneous ice (i.e. sea-ice single crystals) variations in pore morphology induce changes in the aspect ratio by more than 20% about the mean.

Further to these method-related uncertainties is the precise dependence of the permittivity on microstructural variability which is poorly understood at 50 MHz not only in sea ice but in other media with pore fluids (Santamarina and others, 2001). It is not completely understood even in the more studied GHz regime, in which variations for 'flash frozen' sea-water samples of Hoekstra and Cappillino (1971) have been attributed to the expectation of different microstructures. Our single-crystal measurements in NaCl ice indicate a variability in ε' due to crystal anisotropy of only $5 \pm 5\%$. However extrapolating this to estimate the variability on structural grounds in the field measurements is complicated by features of natural sea ice not found in the NaCl single crystals. Further to growth-dependent variations, these include grain boundaries, brine drainage channels, biological matter and variations in all of these due to brine motion. Furthermore, both the hysteresis in our laboratory measurements and the abrupt changes in the spring measurements in Barrow clearly point to the time-varying nature of the microstructure.

7. CONCLUSIONS

Laboratory and field measurements of the relative complex permittivity $\varepsilon = \varepsilon' - j\varepsilon''$ were made with Stevens Water Monitoring Systems Hydra Probes. Care must be taken to ensure reliable probe operation; we suggest independent

https://doi.org/10.3189/002214309788608903 Published online by Cambridge University Press

temperature measurements (at least for calibration). For highly saline environments, we have observed that measurements for $\varepsilon''/\varepsilon' > 3$ are unreliable. The real 'dielectric constant' ε' is physically related to polarization mechanisms, whereas the imaginary 'loss factor' ε'' has an additional contribution from the d.c. conductivity, which for sea ice is highly dependent on the connectivity of brine inclusions. We have inverted an ellipsoidal inclusion model derived from Stogryn (1971), Tinga and others (1973) and Vant and others (1978), to calculate from ε' an apparent inclusion aspect ratio γ, and from ε'' the apparent d.c. conductivity. We find that γ is up to an order of magnitude higher than found in micro-optical studies of sea ice. Scale dependence of microstructural observations and complicated pore morphologies not adequately represented in simplistic pore models likely explain these discrepancies and variability. Modeled polarization mechanisms contribute considerably less to ε'' than the d.c. conductivity. Electrical anisotropy and scale dependence prevent direct comparison with different previous measurements. However, we do see the expected result of higher conductivities than previous, meter-scale, horizontal resistivity measurements at the same location.

Single-crystal measurements showed crystal anisotropy due to brine layering that is weak in ε', but a 20–40% higher value of ε'' when the electric field is parallel to brine layers, rather than perpendicular. Field measurements showed clear signatures of brine motion. Taken together, these results illustrate the variability in the 50 MHz permittivity due to microstructural variability, and suggest that the dual objectives of monitoring microstructural dependence and evolution, and making automated salinity measurements are difficult to uncouple. Field measurements are subject to uncertainties from permittivity measurements, calculated brine volume fractions, and the effect of microstructural variations in what our field measurements suggest may at times be sub-representative sampling volumes. Moreover, these effects are not readily separated. For these reasons, we are unable to derive an accurate inversion of brine volume fraction from field measurements of ε' and ε'', that is, of general, site-independent validity. Hence, hydraprobes seem unsuitable for broad applications in automated salinity measurements, at least in the absence of additional information to help constrain uncertainties in brine volume fraction and inclusion morphology.

The observed fluctuations in ε'' are consistent with salinity variations caused by brine transport over centimeter length scales. We conclude that hydraprobes have proved useful for identifying brine motion in warming ice, and that they may be of value for closer analysis of single-crystal effects on the permittivity, although this would require very careful measurements in association with imaging and microstructural characterization, which is something we are exploring at present.

ACKNOWLEDGEMENTS

This work was supported by the US National Science Foundation. The Barrow Arctic Science Consortium provided logistics support, with valuable field support from H. Ahsoak, S. Oyagak and N. Acker. We thank D. Winebrenner and L. Backstrom for useful discussions. G.D. thanks D. Pavuna of Ecole Polytechnique Fédérale de Lausanne for making possible his visit to Fairbanks. We are grateful to two anonymous reviewers for suggestions and comments.

REFERENCES

Addison, J.R. 1969. Electrical properties of saline ice. *J. Appl. Phys.,* **40**(8), 3105–3114.

Addison, J.R. 1970. Electrical relaxation in saline ice. *J. Appl. Phys.,* **41**(1), 54–63.

Arcone, S.A., A.J. Gow and S. McGrew. 1986. Structure and dielectric properties at 4.8 and 9.5 GHz of saline ice. *J. Geophys. Res.,* **91**(C12), 14,281–14,303.

Backstrom, L.G.E. and H. Eicken. 2006. Capacitance probe measurements of brine volume and bulk salinity in first-year sea ice. *Cold Reg. Sci. Technol.,* **46**(3), 167–180.

Buckley, R.G., M.P. Staines and W.H. Robinson. 1986. In-situ measurements of the resistivity of Antarctic sea ice. *Cold Reg. Sci. Technol.,* **12**(3), 285–290.

Campbell, J.E. 1988. Dielectric properties of moist soils at RF and microwave frequencies. (PhD thesis, Dartmouth College.)

Campbell, J.E. 1990. Dielectric properties and influence of conductivity in soils at one to fifty megahertz. *Soil Sci. Soc. Am. J.,* **54**(2), 332–341.

Campbell, K.J. and A.S. Orange. 1974. The electrical anisotropy of sea ice in the horizontal plane. *J. Geophys. Res.,* **79**(33), 5059–5063.

Cho, H., P.B. Shepson, L.A. Barrie, J.P. Cowin and R. Zaveri. 2002. NMR investigation of the quasi-brine layer in ice/brine mixtures. *J. Phys. Chem. B,* **106**(43), 11,226–11,232.

Cole, D.M. and L.H. Shapiro. 1998. Observations of brine drainage networks and microstructure of first-year sea ice. *J. Geophys. Res.,* **103**(C10), 21,739–21,750.

Cox, G.F.N. and W.F. Weeks. 1983. Equations for determining the gas and brine volumes in sea-ice samples. *J. Glaciol.,* **29**(102), 306–316.

De Loor, G.P. 1968. Dielectric properties of heterogeneous mixtures containing water. *J. Microwave Power,* **3**(2), 67–73.

Eicken, H. 2003. From the microscopic, to the macroscopic, to the regional scale: growth, microstructure and properties of sea ice. *In* Thomas, D.N. and G.S. Dieckmann, *eds. Sea ice: an introduction to its physics, chemistry, biology and geology.* Oxford, Blackwell Publishing, 22–81.

Eicken, H., C. Bock, R. Wittig, H. Miller and H.-O. Poertner. 2000. Nuclear magnetic resonance imaging of sea ice pore fluids: methods and thermal evolution of pore microstructure. *Cold Reg. Sci. Technol.*, **31**(3), 207–225.

Farrelly, B.A. 1982. Comment on the complex-dielectric constant of sea ice at frequencies in the range 0.1–40 GHz. *J. Appl. Phys.,* **53**(2), 1256–1257.

Golden, K.M. and S.F. Ackley. 1980. Modeling of anisotropic electromagnetic reflection from sea ice. *CRREL Res. Rep.* 80-23.

Golden, K.M. and S.F. Ackley. 1981. Modeling of anisotropic electromagnetic reflection from sea ice. *J. Geophys. Res.,* **86**(C9), 8107–8116.

Golden, K.M., S.F. Ackley and V.I. Lytle. 1998. The percolation phase transition in sea ice. *Science,* **282**(5397), 2238–2241.

Golden, K.M., H. Eicken, A.L. Heaton, J. Miner, D.J. Pringle and J. Zhu. 2007. Thermal evolution of permeability and microstructure in sea ice. *Geophys. Res. Lett.,* **34**(16), L16501. (10.1029/2007GL030447.)

Hall, D.L., S. Sterner and R.J. Bodnar. 1988. Freezing point depression of NaCl-KCl-H_2O solutions. *Econ. Geol.,* **83**(1), 197–202.

Hallikainen, M. and D. Winebrenner. 1992. The physical basis for sea ice remote sensing. *In* Carsey, F.D. *and 7 others, eds. Microwave remote sensing of sea ice.* Washington, DC, American Geophysical Union, 29–46. (Geophysical Monograph Series 68.)

Hoekstra, P. and P. Cappillino. 1971. Dielectric properties of sea and sodium chloride ice at UHF and microwave frequencies. *J. Geophys. Res.,* **76**(20), 4922–4931.

Ingham, M., D.J. Pringle and H. Eicken. 2008. Cross-borehole resistivity tomography of sea ice. *Cold Reg. Sci. Technol.*, **52**(3), 263–277.

https://doi.org/10.3189/002214309788608903 Published online by Cambridge University Press

Kawamura, T. 1986. A method for growing large single crystals of sea ice. *J. Glaciol.,* **32**(111), 302–303.

Kovacs, A. and R.M. Morey. 1978. Radar anisotropy of sea ice due to preferred azimuthal orientation of the horizontal C-axes of ice crystals. *J. Geophys. Res.,* **83**(C12), 171–201.

Kovacs, A. and R.M. Morey. 1979. Anisotropic properties of sea ice in the 50- to 150-MHz range. *J. Geophys. Res.,* **84**(C9), 5749–5759.

Langway, C.C., Jr. 1958. Ice fabrics and the universal stage. *SIPRE Tech. Rep.* 62.

Leppäranta, M. and T. Manninen. 1988. The brine and gas content of sea ice, with attention to low salinities and high temperatures. Helsinki, Finnish Institute of Marine Research. (Internal Report 88-2.)

Light, B., G.A. Maykut and T.C. Grenfell. 2003. Effects of temperature on the microstructure of first-year Arctic sea ice. *J. Geophys. Res.,* **108**(C2), 3051. (10.1029/2001JC000887.)

Morey, R.M., A. Kovacs and G.F.N. Cox. 1984. Electromagnetic properties of sea ice. *CRREL Rep.* 84-2.

Notz, D., J.S. Wettlaufer and M.G. Worster. 2005. A non-destructive method for measuring the salinity and solid fraction of growing sea ice in situ. *J. Glaciol.,* **51**(172), 159–166.

Perovich, D.K. and A.J. Gow. 1996. A quantitative description of sea ice inclusions. *J. Geophys. Res.,* **101**(C8), 18,327–18,343.

Pringle, D.J., H. Eicken, H.J. Trodahl and L.G.E. Backstrom. 2007. Thermal conductivity of landfast Antarctic and Arctic sea ice. *J. Geophys. Res.,* **112**(C4), C04017. (10.1029/2006JC003641.)

Santamarina, J.C., K.A. Klein and M.A. Fam. 2001. *Soils and waves: particulate materials behavior, characterization and process monitoring.* Chichester, Wiley.

Seyfried, M.S. and M.D. Murdock. 2004. Measurement of soil water content with a 50-MHz soil dielectric sensor. *Soil Sci. Soc. Am. J.,* **68**(2), 394–403.

Seyfried, M.S., L.E. Grant, E. Du and K. Humes. 2005. Dielectric loss and calibration of the Hydra Probe soil water sensor. *Vadose Zone J.,* **4**(4), 1070–1079.

Stevens Water Monitoring Systems. 2005. *Hydra Probe preliminary instruction manual.* Portland, OR, Stevens Water Monitoring Systems, Inc.

Stogryn, A. 1971. Equations for calculating the dielectric constant of saline water. *IEEE Trans. Microwave Theory Tech.,* **19**(8), 733–736.

Timco, G.W. 1979. An analysis of the *in-situ* resistivity of sea ice in terms of its microstructure. *J. Glaciol.,* **22**(88), 461–471.

Tinga, W.R. and W.A.G. Voss. 1973. Generalized approach to multiphase dielectric mixture theory. *J. Appl. Phys.,* **44**(9), 3897–3902.

Vant, M.R., R.O. Ramseier and V. Makios. 1978. The complex-dielectric constant of sea ice at frequencies in the range 0.1–40 GHz. *J. Appl. Phys.,* **49**(3), 1264–1280.

Weeks, W.F., S.F. Ackley and D.F. Blossey. 1986. The growth, structure, and properties of sea ice. *In* Untersteiner, N., *ed. Geophysics of sea ice.* London, etc., Plenum Press, 9–164. (NATO ASI Series B: Physics 146.)

Yoshikawa, K., P.P. Overduin and J.W. Harden. 2004. Moisture content measurements of moss (*Sphagnum* spp.) using commercial sensors. *Permafrost Periglac. Process.,* **15**(4), 309–318.

MS received 21 February 2008 and accepted in revised form 15 August 2008